

JGR Atmospheres

RESEARCH ARTICLE

10.1029/2019JD031453

Key Points:

- The first observations of thunder-induced seismic waves are by the distributed acoustic sensing (DAS) array with preexisting telecommunication fiber optics
- Dense DAS data reveal the characteristics of thunder-seismic signals and enable seismic full waveform analysis to conduct
- A positive correlation between DAS seismic wave power and lightning current power was found

Supporting Information:

- Supporting Information S1

Correspondence to:

T. Zhu,
tyzhu@psu.edu

Citation:

Zhu, T., & Stensrud, D. J. (2019). Characterizing Thunder-Induced Ground Motions Using Fiber-Optic Distributed Acoustic Sensing Array. *Journal of Geophysical Research: Atmospheres*, 124, 12,810–12,823. <https://doi.org/10.1029/2019JD031453>

Received 31 JUL 2019

Accepted 9 NOV 2019

Published online 11 DEC 2019

Characterizing Thunder-Induced Ground Motions Using Fiber-Optic Distributed Acoustic Sensing Array

Tieyuan Zhu¹ and David J. Stensrud²

¹Department of Geosciences, The Pennsylvania State University, University Park, PA, USA, ²Department of Meteorology and Atmosphere Science, The Pennsylvania State University, University Park, PA, USA

Abstract We report for the first time on a distributed acoustic sensing (DAS) array using preexisting underground fiber optics beneath the Penn State campus for detecting and characterizing thunder-induced ground motions. During a half-hour interval from 03:20–03:50 UTC on 15 April 2019 in State College, PA, we identify 18 thunder-induced seismic events in the DAS array data. The high-fidelity DAS data show that the thunder-induced seismics are very broadband, with their peak frequency ranging from 20 to 130 Hz. We use arrival times of the 18 events to estimate the phase velocity of the near surface, the back azimuth, and location of thunder-seismic sources that are verified with lightning locations from the National Lightning Detection Network. Furthermore, the dense DAS data enable us to simulate thunder-seismic wave propagation and full waveform synthetics and further locate the thunder-seismic source by time-reversal migration. Interestingly, we found that thunder-seismic power recorded by DAS is positively correlated with National Lightning Detection Network lightning current power. These findings suggest that fiber-optic DAS observations may offer a new avenue of studying thunder-induced seismics, characterizing the near-surface velocity structure, and probing the thunder-ground coupling process.

Plain Language Summary Detailed understanding of how weather processes in the atmosphere couple into seismic waves in the solid Earth is extremely important and will require a high-resolution observation of this coupling in the temporal and spatial scales. This study is the first to demonstrate the use of preexisting telecommunication fiber optics beneath the Penn State campus to characterize thunder-induced seismic waves in the near surface. The fiber-optic array is composed of up to tens of kilometers of fiber-optic cable and can achieve the high resolution at the scale of meters. The high-fidelity distributed acoustic sensing (DAS) data can provide a detailed characterization of thunder-induced signals and further track thunder-induced sources. Moreover, this is the first study to demonstrate the relationship between thunder current energy and DAS recorded ground motion power, suggesting the DAS observations can be useful for characterizing thunder-ground motions and probing the complex thunder-ground coupling process.

1. Introduction

Extreme weather events (such as hurricanes and thunderstorms) can lead to substantial societal impacts, including damage to buildings and other infrastructure, global economic loss, and human injuries and fatalities. Those events often transfer their energy to the solid Earth subsurface to excite seismic waves. Seismologists have shown evidence of hurricane-generated seismic signals in the oceans (e.g., Gerstoft et al., 2006; Gualtieri et al., 2018) and on land (e.g., Ebeling & Stein, 2011; Tanimoto & Lamontagne, 2014). Hurricane-generated seismic signals allow seismologists to detect and track large hurricanes and their intensity (e.g., Gerstoft et al., 2006; Retailleau & Gualtieri, 2019) and are used as seismic sources to characterize the elastic properties (i.e., wave speed) of Earth structures (Lin & Langston, 2007; Zhang et al., 2010). Moreover, this energy transfer process between weather process and solid Earth can be complex (nonlinear and frequency dependent; Gualtieri et al., 2018) and likely varies on a wide range of temporal and spatial scales. Therefore, detailed understanding of how weather processes in the atmosphere couple into seismic waves in the solid Earth is extremely important and requires a high-resolution observation of this coupling in the temporal and spatial scales. In this study we present a seismological observation of the thunderstorm-induced energy as an example to demonstrate that a fiber-optic distributed acoustic sensing (DAS) array that has a spatial resolution at the meter scale and continuous temporal samplings can be useful to fully

characterize thunder-induced ground motions and may serve as a useful data source to determine the velocity structure of the near surface and probe the coupling relationship between thunderstorms and solid Earth.

Physically, thunder shock waves generated from lightning propagate through the air. Recordings of acoustics can be used to reconstruct the geometry of lightning using a microphone array (Few, 1969, 1970). The infrasound thunder signals have been observed and located with microphones and microbarometers (e.g., Assink et al., 2008; Farges & Blanc, 2010). Lacroix et al. (2018) used a 50-m triangular array of four recalibrated microphones sampled at 500 Hz and detected thunder recordings in the [0.1–180]-Hz frequency bandwidth within the [0.3–20]-km distance. The characteristics (movement and acoustic pressures) of thunderstorms have been shown using observations from microphones and microbarometers (Assink et al., 2008; Farges & Blanc, 2010; Lacroix et al., 2018). These acoustic waves can transfer sufficient pressure changes to induce ground motion and produce an air-coupled Rayleigh wave propagating in the near surface (Lin & Langston, 2007). Thus, broadband seismometers can record the thunder-induced ground motion signals that can further be used to characterize the thunder source. For example, Kappus and Vernon (1991) analyzed the acoustic signature of thunder from two seismometers to distinguish two thunder patterns where the frequency acoustic thunder signals (peaks at 25–55 Hz) are possibly generated by cloud-to-ground lightning stroke. Lin and Langston (2007, 2009a) investigated infrasonic thunder-induced ground motions using a small seismometer-microphone array. They performed a time domain grid search to constrain the azimuth and apparent velocity of two typical thunder events, but the limited-aperture array geometry was inadequate to track and characterize the source. To improve the source characterization, a wide-aperture and dense seismic array having multiple sensors (in the order of tens or hundreds) is essential (Zhu et al., 2019).

Recent development of the DAS interrogator technology enables us to convert the telecommunication fiber-optic cables to an array of acoustic sensors that provides continuous measurements of dynamic strain fields in space and time. The feasibility of DAS arrays for recording ground vibrations has been demonstrated in active-source seismic surveys (Daley et al., 2013; Mateeva et al., 2014), ambient noise monitoring (Dou et al., 2017; Martin et al., 2018; Zeng et al., 2017), and earthquake detection (Ajo-Franklin et al., 2019; Lindsey et al., 2017; Wang et al., 2018; Yu et al., 2019). Compared to seismometers, the DAS array is composed of up to tens of kilometers of fiber-optic cable and is transformed into thousands of virtual sensors with spatial sampling along the cable on the scale of meters. Such spatially dense data enable sophisticated exploration seismology methods to process the DAS data, for example, full waveform migration and inversion (Egorov et al., 2018). Moreover, recent studies demonstrate that telecommunication optical-fiber cable networks widely installed in recent decades can be used for DAS recording (Jousset et al., 2018; Martin et al., 2018). Both Ajo-Franklin et al. (2019) and Yu et al. (2019) demonstrated the value of a 20-km-long DAS array using telecommunication fiber optics for recording ambient noise and earthquakes in California. Thus, if thunder-induced seismic waves can be detected by the DAS fiber-optic array, the high-fidelity DAS data would be able to provide the detailed characterization of thunder-induced ground motions in a local area.

Here we report for the first time observations of thunder-induced ground motions using the DAS fiber-optic array that is part of the Fiber Optic for Environmental SENSEing (FORESEE) project on the Penn State campus. A half-hour of DAS data measurements was recorded during thunderstorms on 15 April 2019 in State College, PA. We analyze these dense arrival time measurements to determine horizontal phase velocity and back azimuth using a time domain grid search using dense arrival time measurements. We then invert for the thunder-seismic source location and its origin time using a least squares inversion. Taking advantage of the high-density sensors, we also conduct full waveform modeling and time-reversal source imaging analysis of the thunder-seismic waveforms.

2. Data

2.1. Penn State Fiber-Optic DAS Array Installation and Calibration

Starting on 5 April 2019, a DAS array was initialized using a spare optical fiber in an existing telecommunication cable run underneath the Penn State University campus (Figure 1a). The existing fiber cable for telecommunications is directly laid in the concrete conduit at a depth of about 1 m (Figure 1b). The DAS measurements are recorded by the Silixa iDAS2 interrogator unit, which is connected to one end of the fiber using an E2000 APC connector. The other end was terminated to create high loss and prevent a large-amplitude back reflection from this far end of the fiber. The DAS array made continuous strain rate

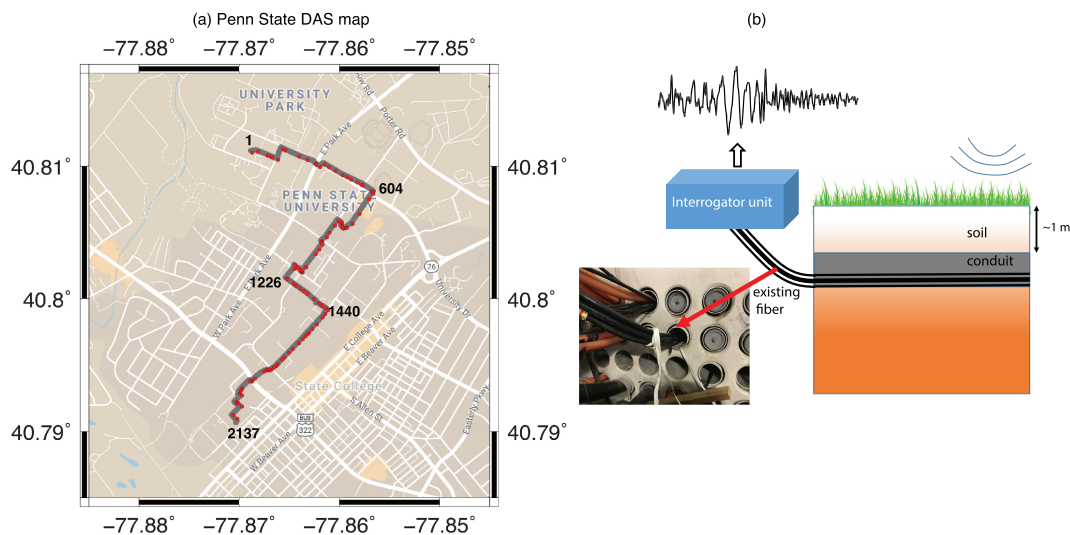


Figure 1. (a) Penn State fiber-optic distributed acoustic sensing (DAS) array map. Red dots indicate our tap test locations. Five channel numbers are listed. (b) Cartoon of DAS array connecting existing fiber optics. The left-bottom subfigure shows the preexisting fiber-optic cable (in black) used for this project.

measurements at a 500-Hz sampling frequency with a 10-m gauge length along the fiber. Similar to geophone sensing of particle velocity, DAS sensing of the strain rate shows the similar angular sensitivity to Rayleigh waves and the peak sensitivity appears when the wave propagation direction is parallel to the DAS array (Martin et al., 2019). Here the channel spacing is 2 m, which is much denser than the typical seismic geophone arrays. This results in 2,137 channels (sensors) over 4,274 m. The locations for 2,137 channels are determined from tap tests.

With the knowledge of the fiber cable path along the conduit and telecommunication holes provided by Penn State Enterprise Networking & Communication Services department, we ran tap tests to determine the GPS position of the representative channels (see Figure 1a). For each tap test, we use a hammer source to generate six distinguished shots on the ground and ideally the center channel of shots will correspond to the GPS position of the hammer source. One example of the raw DAS recordings $u(x, t)$ is shown in Figure 2a. The six hyperbolas are fairly clean. In many cases, the raw DAS data contaminated by strong background noise brings difficulties to identify the hammer shots. Instead, we compute the spectral energy $E(x, T) = \sum_f$

$\tilde{u}(x, f)$, where $\tilde{u}(x, f)$ is the Fourier transform of windowed $u(x, t)$ by a short sliding window. The window size is 255 samples. As seen in Figure 2b, the hammer shots are easily identified and the center is relatively unambiguous. After 101 tap tests, we determined the positions of 101 channels. We then interpolated those to the 2,137 channels.

In the calibration procedure, raw DAS measurements (counts) are first scaled to strain rate by multiplying a system scale factor (116 nm) and sampling frequency (500 Hz) and dividing gauge length (10 m), resulting in strain rate (nanostain/s) along the fiber. Several authors calibrate strain rate by standard seismometer particle displacement or velocity measurements (Daley et al., 2016; Lindsey et al., 2017; Spikes et al., 2019; Wang et al., 2018; Yu et al., 2019). Here the strain rate is converted to the acceleration data based on a proportional relation between the strain rate and acceleration $\dot{\epsilon} \propto \pm \frac{1}{c} \ddot{u}$ (Daley et al., 2016), where $\dot{\epsilon}$, \ddot{u} , and c are the strain rate, acceleration, and apparent wave propagation velocity along the fiber. Without the information of propagation velocity c , we multiplied a gain factor of 5 to DAS data to match with the acceleration waveform (Lindsey et al., 2017).

Figure 3a shows an example of the hammer shot to excite the active-source energy above the fiber path. After synchronizing the GPS timing, direct P wave (~ 1.2 km/s) can be clearly identified (black dashed line) in DAS (Figure 3a). It is a typical P wave velocity in the shallow geologic structure. We also identify many traffic signals. For example, Figure 3b shows car signals, where the passing speed is calculated by the slope of the signal. Figure 3c shows the comparisons of the three-component seismograms (acceleration in

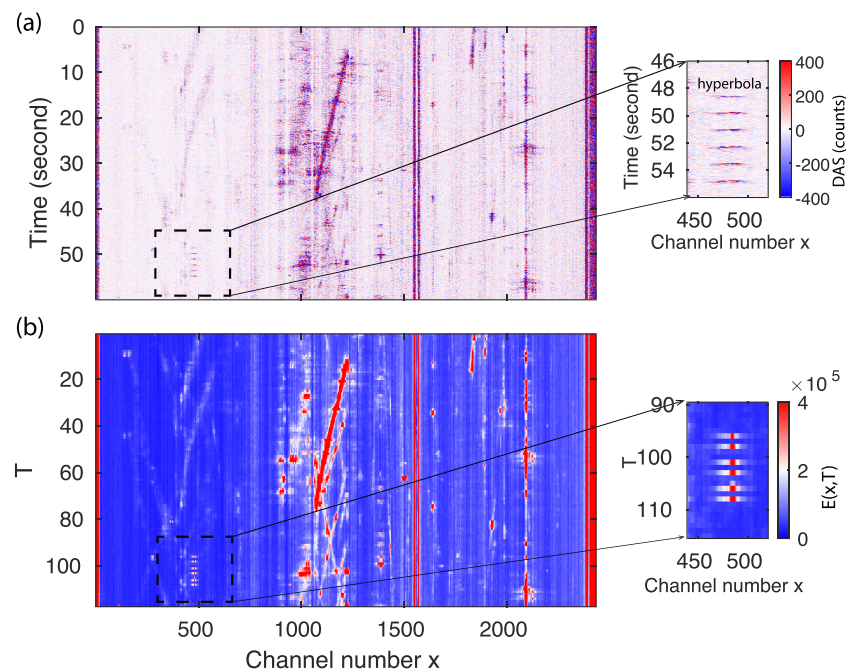


Figure 2. (a) The DAS recording of a tap-testing shot on the ground and its zoom-in section around six shots. (b) Spectral energy $E(x,T)$ and its zoom-in section around six shots for searching the shot location.

micrometers per square second) from the closest broadband seismometer (PSRS, about 10 km away from the fiber) with DAS waveform data (Channel 400) after applying a band-pass filter 0.05–1.0 Hz. It is clear that the DAS data show an agreement with the reference seismogram (particularly S wave in the E component). One possible reason for inconsistent DAS coda wave amplitudes is that the DAS data represent the average signals over the gauge length instead of a point sensor like the geophone (Wang et al., 2018), although many other factors may play a role in waveform differences, for example, the distance of seismic station and DAS array, directional sensitivity, and the host environment.

2.2. DAS Recordings of Thunder

In this report, we focus on high signal-to-noise ratio seismic signals generated by a severe thunderstorm that passed over State College between 03:20 and 03:50 UTC on 15 April 2019. In this 30-min interval of DAS data, we manually identify 18 seismic events. Figure 4a shows three examples of DAS recordings at 2,137 channels of the fiber-optic DAS array after band-pass filtering [1–200] Hz (the rest of events are shown in Figure 5). Although some particular channels show strong horizontal noise (e.g., cars near Channels 1650–1800 during Events e8, e9, and e10), coherent arrivals above the noise level throughout the array are easily identified and labeled. First, the arrival times of those events vary with offset throughout all parts of the array (channel number), suggesting that thunder-seismic sources are likely close to the DAS array. Second, it is interesting to note that the amplitudes of Events e4 and e8 show a substantial variation across channel number, due to wave geometry spreading effects or physical wave attenuation in the near-surface layers. The waveform of the Event e8 is relatively impulsive while e4, e6, and e10 last longer (~3 s) and have multiple claps in the 3-s waveforms. In the spectrogram of two DAS traces (Channels 400 and 2000; Figure 4), we can see that waveforms of e4 are dispersive where high frequencies are more attenuated around Channel 2000 than around Channel 400, suggesting that the vibrations recorded are dispersive surface waves as opposed to nondispersive air waves. Dispersive amplitudes might be caused by the near-surface high attenuation materials (e.g., unconsolidated soils) around Channel 2000. It is also worth noting that amplitude spectra across the channels for e4 and e8 show a clear variation in Figure 6, in particular the abrupt change at Channel 1438 that is approximately the turning point (see the fiber map Figure 1a) may indicate the near-surface geology variation. Figure 7 compares the stacked DAS trace of e6 with the seismogram recorded by the nearby Seismic Station PSRS ([15–40 Hz] band-pass filtering), which shows a 29-s time

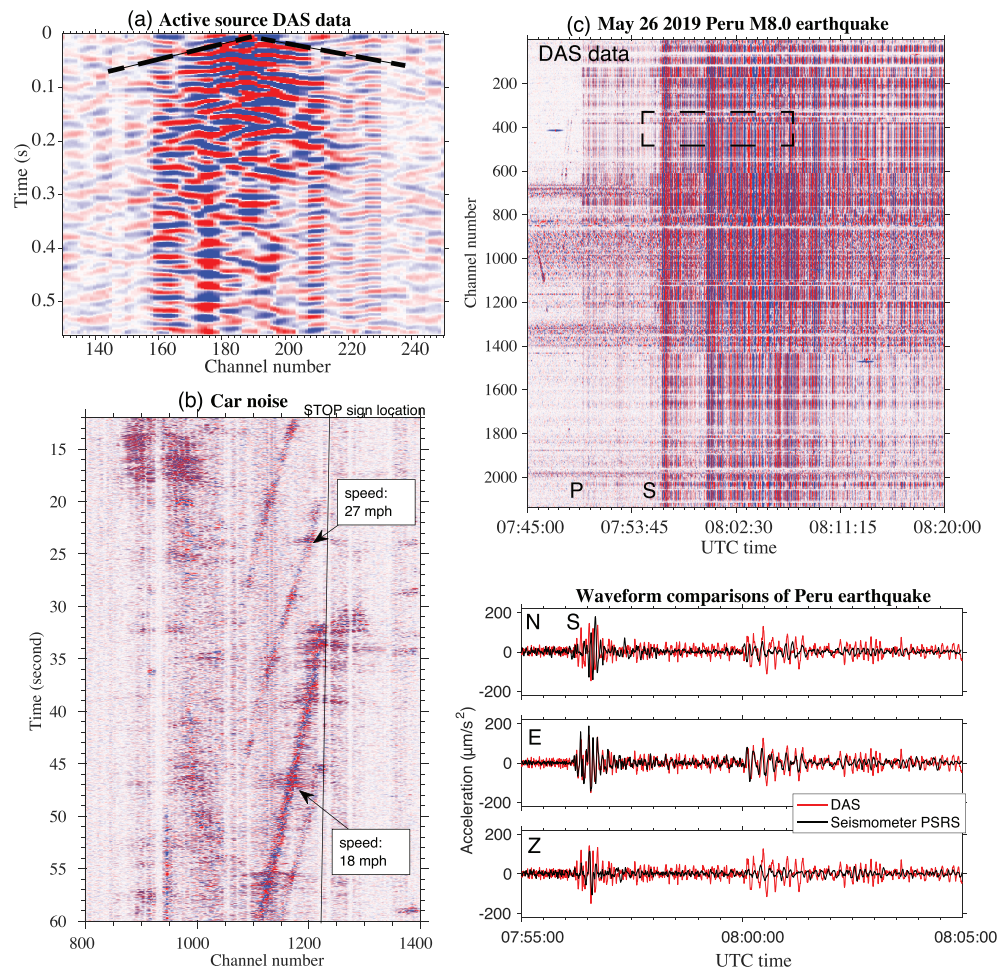


Figure 3. DAS recordings of (a) hammer active-source signals, (b) traffic car signals, and (c) Peru M8.0 earthquake on 26 May 2019. In the active-source data, direct *P* wave (~ 1.2 km/s) can be clearly identified (black dashed line). For car signals, the passing speed is calculated by the slope of the signal, where channel spacing is 2 m. In (c), for the comparison, we plot the three-component seismograms (acceleration in micrometers per square second) from the closest broadband seismometer (Station PSRS) with DAS waveform data (Channel 400 by band-pass filter 0.05–1.0 Hz).

delay for sound traveling at 340 m/s over 10 km from the DAS array. Although we did not attempt to match the waveform, the seismogram shows multiple arrivals at the same timing corresponding to multiple claps of thunder (arrows in Figure 7). The multiple-claps features are also illustrated in an animation of one channel (03:34–03:35 UTC) in <https://sites.psu.edu/tzhu/foresee/>.

In addition, the spectrogram plots show that each individual clap of thunder is very broadband (Figures 4 and 7c). The power spectra of most of those events show considerable energy up to the Nyquist frequency. These frequencies of thunder signals are consistently above the background noise level with a fairly good signal-to-noise ratio and fall off after 150 Hz (Figure 7c). The frequency of thunder signals peaks from 20 to 130 Hz, which is consistent with previously published values for thunder signals associated with lightning stroke by microphones (Few, 1969; Holmes et al., 1971; Lacroix et al., 2018) and is apparently wider than seismometer's recordings (Kappus & Vernon, 1991).

3. Characterizing the Thunder-Seismic Events

To characterize these events, we first use the arrival times of each event at all channels to find the event back azimuth and apparent slowness using a time domain grid search technique. We assume a plane wave traveling across the array. Let t_i be the arrival time picked at sensor i , and t_{ref} be the arrival time at the reference sensor, then $\Delta t_i = t_i - t_{ref}$ is the observed time delay at sensor i . The grid search method is used to

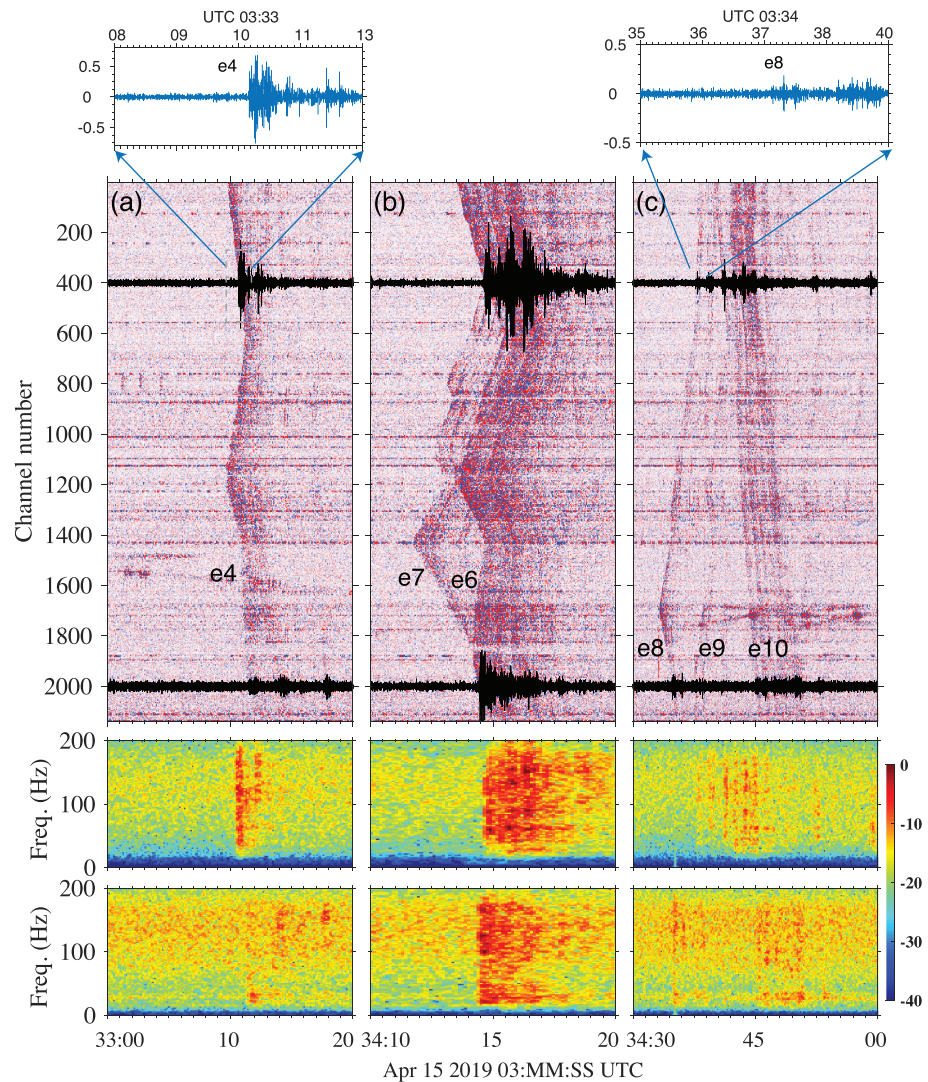


Figure 4. DAS array observations of several thunder-induced seismic events on 15 April 2019 in State College, PA. Two traces (Channels 400 and 2000) are overlaid. We filtered DAS data by the Butterworth band-pass filter (1–200 Hz). Lower panels show DAS spectrograms (dB) computed for Channel 400 and Channel 2000, respectively. (a) Event e4, (b) Events e6 and e7, and (c) Events e8, e9, and e10.

minimize the residual between observations Δt and the calculated delay times by optimizing the horizontal components of the slowness s . The objective function of the grid search method is defined as

$$\min \left| \sum_{i=1}^N t_i - d_i s \right| \quad (1)$$

where N is the number of sensors, d_i is the projected distance between the reference sensor, and i sensor with the incident wave vector and is given by

$$d_i = x_i \sin \theta + y_i \cos \theta \quad (2)$$

and θ is the backazimuth of the wave vector and x_i and y_i are coordinates of sensor i .

We first calculate the travel time from a grid point to a station simply by dividing the distance between them by a constant horizontal phase velocity (1/s). To estimate errors for the ray parameter and back azimuth, we apply a Monte Carlo error propagation technique with a 2-s (± 1 s) Gaussian random error to observed arrival times. The slowness-azimuth grid search results include the slowness, back azimuth, and their uncertainties.

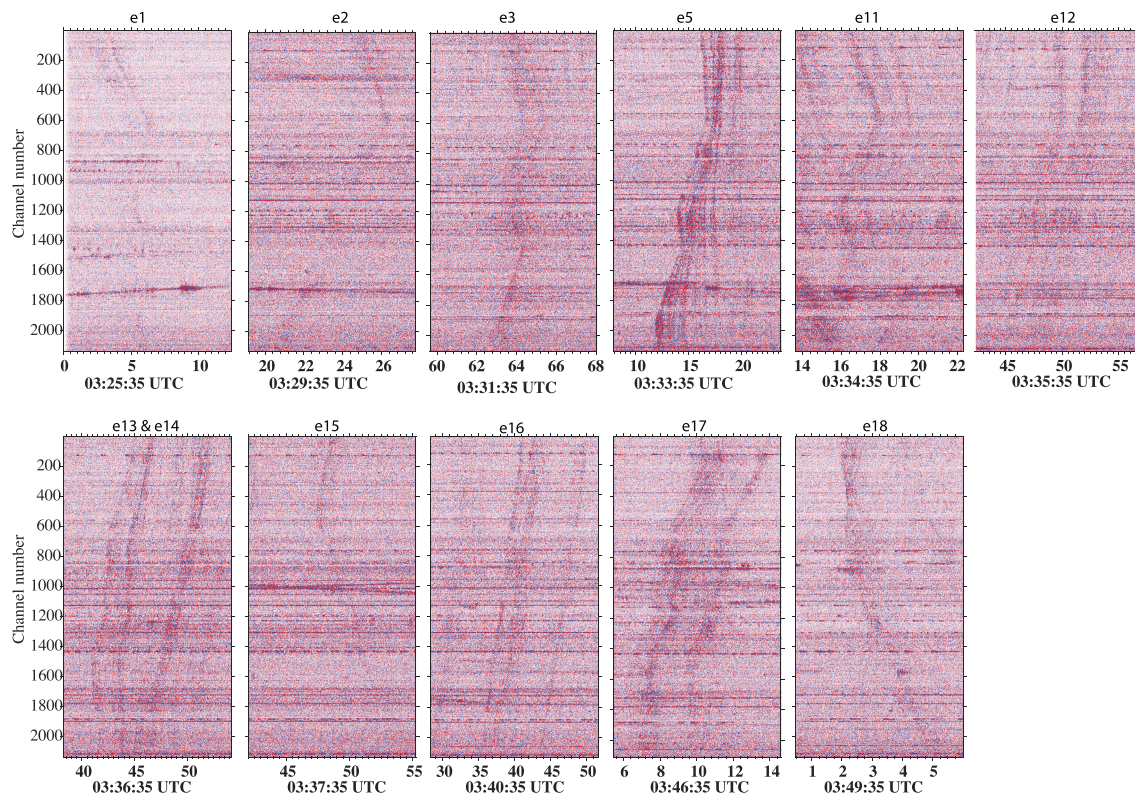


Figure 5. DAS recordings of the 18 seismic events during 03:20–03:50 UTC 15 April 2019. Events e4 and e6–e10 are pictured in Figure 4.

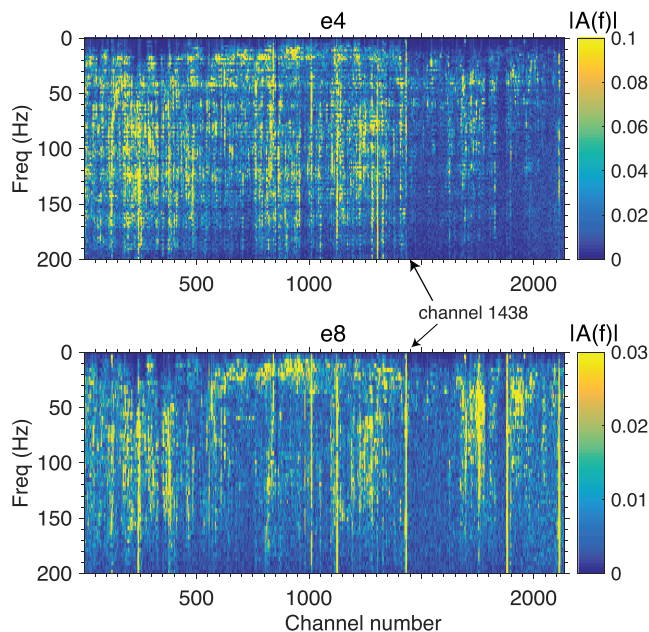


Figure 6. Amplitude spectra of Events e4 and e8 across the DAS array. The black arrows indicate the Channel 1438 that is near a crossing point of the array (Figure 1a).

Next, we use the modified Geiger's method (Menke, 2012) to determine the event location, its origin time, and wave velocity. The idea is that a given trial solution of unknowns (event location and origin time) is updated by minimizing the least square misfit of the observed and predicted arrival times across all stations. Since the origin time is unknown, the observed arrival times t_{obs} for each event are chosen as $t_{obs} - \min(t_{obs})$. The initial locations (x, y) for each event are randomly chosen as $x, y \in [-10, 10]$ km and $t_0 = 1$ s. The initial velocity v_0 is adopted from the above grid search results. Because the source is assumed at the ground surface, no elevation z is estimated. Then, we analyze a set of possible propagation velocities using a grid search over $[v_0 - 0.1 \text{ km/s}, v_0 + 0.1 \text{ km/s}]$ to minimize the arrival time residuals to find the corresponding best fit source locations. Figure 8 shows the root-mean-square (RMS) arrival time residual maps of four events from the azimuth-slowness grid search and least squares location inversion (LSLI). In the RMS map with the axes of slowness and azimuth, the lowest RMS is considered as the solution and the vicinity of the point with the lowest RMS gives an indication of the uncertainty of estimates. For example, both Events e1 and e6 have a large uncertainty in the slowness, whereas e12 and e16 constrain the slowness better. All calculated values (back azimuth, slowness, locations, and initial times) are summarized in Table 1.

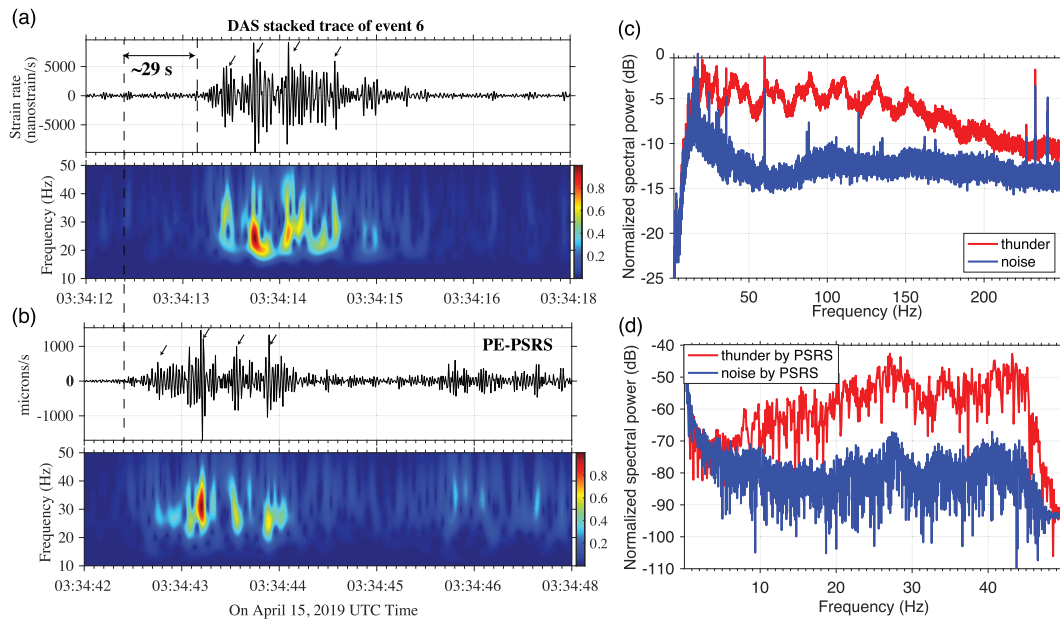


Figure 7. (a) Stacked DAS traces of Event e6 after aligning the event based on picked arrival time. Below is the time-frequency representation of the stacked trace using the S-transform. (b) Recorded trace from nearby Seismic Station PSRS (~10 km away from the DAS array) and its time-frequency map. (c) DAS power spectra of unfiltered Events e6 and e7 data (15-s time series around the e6 signal (red line) compared with a background noise window (blue line) measured by all DAS channels. (d) Signal and noise power spectra of unfiltered PSRS seismometer recording.

The updated velocity for each event is comparable to the value obtained from slowness-azimuth results shown in Figure 9a. We find that the apparent velocity of all signals is 325–970 m/s and averaged at 440 m/s. This implies that most of the recorded waves are not direct air waves and are likely to be the air-coupled Rayleigh wave caused by the trapped propagating wave in the substrate layer (Lin & Langston, 2009b).

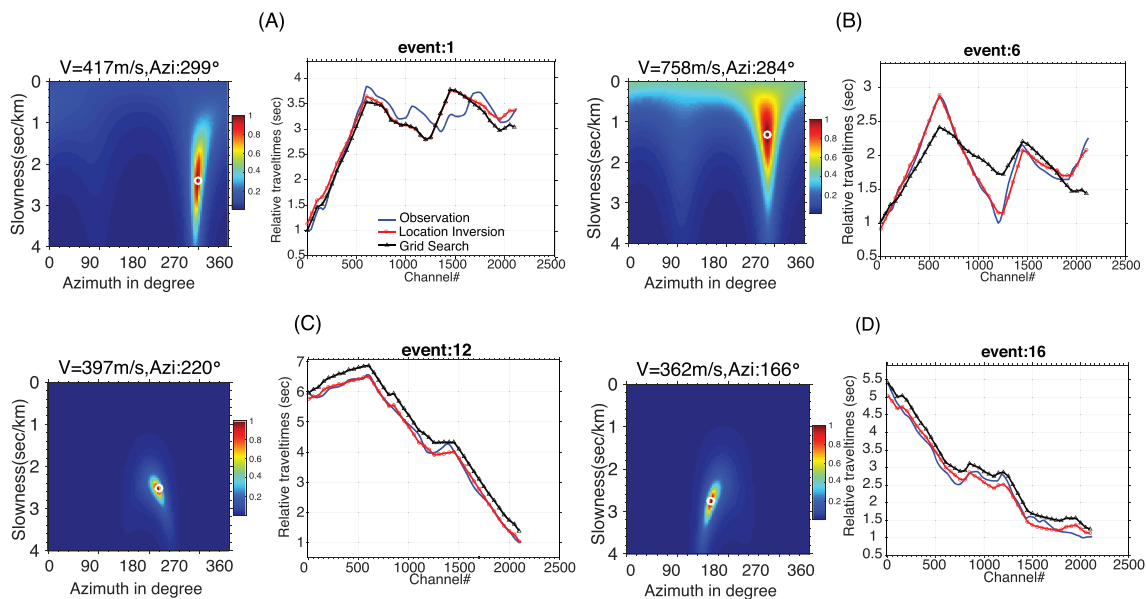


Figure 8. Slowness and azimuth computed by the grid search for Events e1, e6, e12, and e16. The time domain grid search (TDGS) contours are defined in normalized 1 over RMS residual. The optimal slowness-azimuth solutions for selected events are indicated by white circles. For each event, we also compare the observed arrival time (blue) and the predicted ones (black) by the TDGS. The red line represents the arrival time predicted by the LSLI. For Event e6, it is clear that the arrival times by the LSLI better match the observed ones than TDGS. This can be explained that when the event is close to the array the plane wave assumption for the grid search will not be satisfied.

Table 1
Source Parameters of Thunder-Induced Signals

Events	Azimuth (°)	Slowness (s/km)	Slowness by LS (s/km)	$x + \text{std}$ (km)	$y + \text{std}$ (km)	t_0 (s)	initial time (MM:SS)
e1	284 ± 0.6	1.80	2.25	-4.41 ± 0.20	4.00 ± 0.22	-10.7	25:28
e2	230 ± 0.1	2.65	2.63	-3.60 ± 0.03	-2.41 ± 0.17	-10.4	29:46
e3	277 ± 0.2	1.30	1.29	-5.50 ± 0.10	1.82 ± 0.02	-6.8	32:31
e4	313 ± 0.3	0.85	2.28	-0.13 ± 0.01	1.62 ± 0.00	-0.6	33:08
e5	190 ± 0.1	2.95	2.24	0.25 ± 0.11	-0.59 ± 0.22	-4.0	33:44
e6	284 ± 0.2	2.38	2.07	-0.68 ± 0.00	1.52 ± 0.00	-3.48	34:12
e7	111 ± 0.5	3.25	2.80	1.11 ± 0.04	0.92 ± 0.01	0.38	34:13
e8	162 ± 0.7	2.45	2.20	0.50 ± 0.32	0.53 ± 0.00	-0.9	34:34
e9	244 ± 0.2	2.20	3.08	-3.62 ± 0.02	-0.69 ± 0.02	-7.6	34:28
e10	0 ± 0.4	1.40	1.35	0.68 ± 0.18	6.28 ± 0.29	-4.4	34:39
e11	255 ± 0.2	2.20	2.28	-3.90 ± 0.34	0.05 ± 0.33	-7.7	34:42
e12	93 ± 0.5	2.60	2.57	-2.97 ± 0.00	-2.83 ± 0.18	-3.0	36:11
e13	219 ± 0.1	2.50	2.00	1.99 ± 0.29	-1.31 ± 0.10	-5.7	36:14
e14	133 ± 0.6	3.10	3.00	2.76 ± 0.06	-1.16 ± 0.01	-7.1	37:09
e15	40 ± 0.4	2.90	2.80	4.20 ± 0.00	6.22 ± 0.00	-9.6	38:13
e16	165 ± 0.7	2.75	2.73	1.50 ± 0.10	-3.06 ± 0.11	-8.2	41:03
e17	144 ± 0.6	2.55	2.40	4.16 ± 0.11	-4.35 ± 0.23	-14.6	46:28
e18	29 ± 0.5	1.20	1.43	2.65 ± 0.05	5.53 ± 0.45	-5.8	49:32

Figure 9b plots the back azimuth (relative to the center point of the fiber array) of all events from the azimuth-slowness grid search, overlaying the back azimuth of lightning strike data provided by the National Lightning Detection Network (NLDN). The NLDN mainly measures electromagnetic waves and

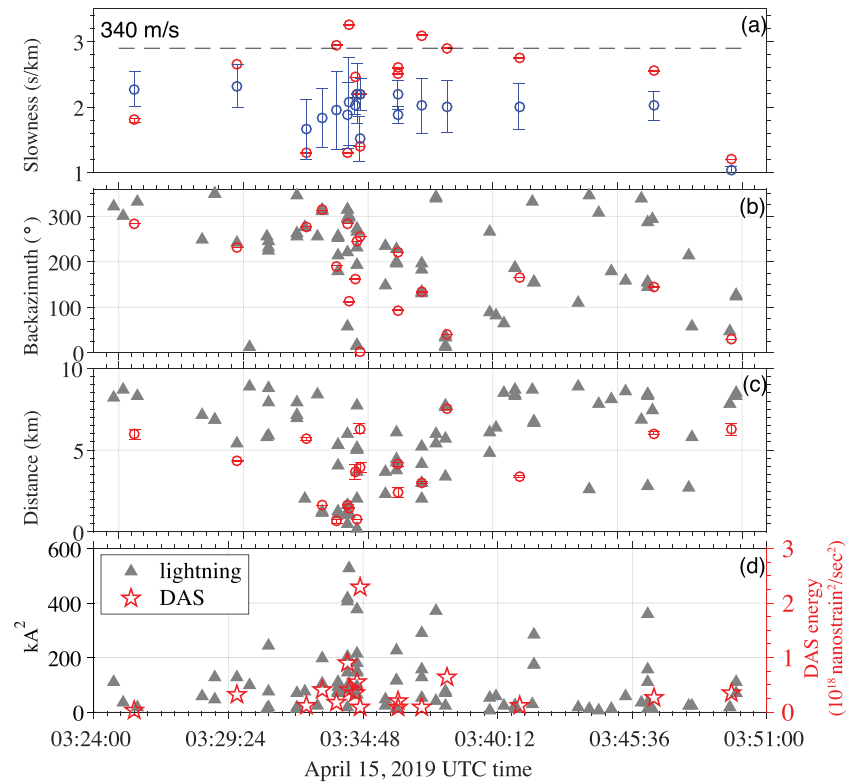


Figure 9. (a) Slowness, (b) back azimuths, and (c) distance of seismic events from the center of the DAS array during 03:20–03:50 UTC on 15 April 2019. Gray triangles are calculated from the lightning strike locations relative to the center of the DAS array. In (a), the red circles are the estimation of slowness from the azimuth-slowness grid search, while the blue from the location inversion. (d) compares DAS signal power E_{DAS} of events to the lightning current energy that is the squared peak current (kA^2).

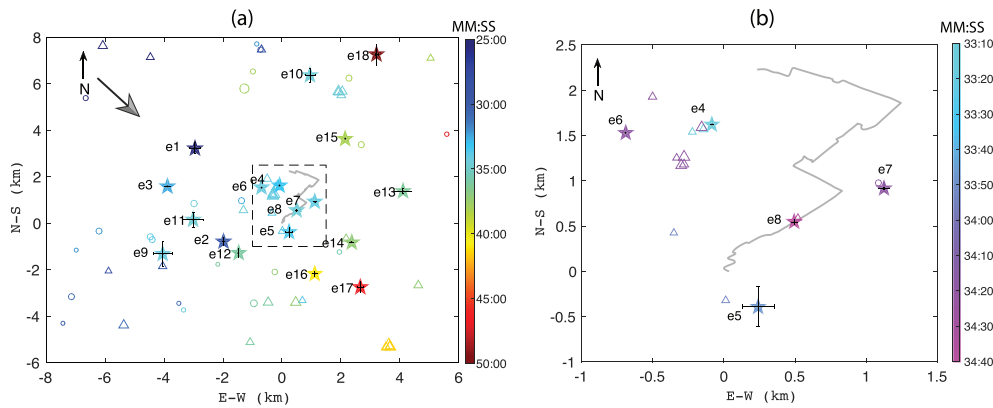


Figure 10. (a) Seismic event locations from the DAS array observation (star) are compared to lightning striking locations (cloud-to-ground stroke in triangles and cloud-to-cloud stroke in circles) from NLDN during 03:25–03:50 UTC on 15 April 2019 in State College, PA. The movement direction is indicated by the arrow. The circle size is dependent on the lightning striking peak amplitude. The larger marker means the stronger strike. The contour lines indicate the time. (b) Zoomed locations for five events (e4, e5, e6, e7, and e8) around the DAS array.

uses the time-of-arrival approach to yield cloud-to-ground flash detection efficiencies of over 90% and location accuracies of better than 200 m (Murphy, 2018; Nag et al., 2015). The uncertainty in resolved back azimuths is estimated less than $\pm 1^\circ$. Back azimuths detected by DAS correlate very well with lightning strike data, indicating that the thunder-induced seismic sources moved from larger back azimuth to small back azimuth (from the northwest to the southeast), which implies the thunderstorm movement. Figure 9c shows the distance of 18 events to the center of the DAS array (defined at Channel 1226). One can see that the thunderstorm approaches the DAS array and is over the array around 03:34 UTC before moving away. This also explain that the events around 03:34 exhibit larger amplitudes (Figures 4 and 5).

The total seismic energy received at all DAS fiber sensors over the signal duration T is

$$E_{DAS} = \sum_{i=1}^N \int_{t_0}^{t_0+T} d^2(r_i, t) dt \quad (3)$$

where d is the DAS strain rate measurement (unit: nanostrain/s) at sensor r_i , i is the sensor index (N sensors), and t_0 is the first arrival time of the thunder signal at the sensor r_i . To select the first arrival waveform, T is chosen as 0.25 s.

Figure 9d shows the comparison of stacked DAS seismic energy E_{DAS} (nanostrain²/s²) and lightning current power (kA²). We can see that there seems to exist a correlation of two data (triangles vs stars), although they have very different units. Interestingly, the peak of E_{DAS} more or less coincides with the peak power of lightning around 03:34 UTC when the lightning is passing the array. In another word, the stroke with large current power induced strong ground motions that induced large DAS energy. Note that the DAS seismic energy could be also influenced by near-surface heterogeneities (scattering and attenuation) along the wave propagation path, given that the distances of DAS events and lightning stroke from the array peak around 03:34 UTC (Figure 9c).

The best fit locations for the 18 events are shown in Figure 10 as stars. The color bar indicates the events' initial times. The error bars indicate the standard deviation of each location with respect to the velocity uncertainty ± 0.1 km/s. To evaluate the location, we draw reference lightning striking locations (no elevation information) from NLDN (please find the complete lightning stroke information in the supporting information). We can see from Figure 10 that the location error (indicated by black crosses) is proportional to the distance from the array, that is, the smaller the error the closer to the array, vice versa. It is worth noting that the distant sources from the DAS array are not well constrained probably due to a narrower aperture of the DAS array relative to the distribution of the sources. Another reason for deviations could be the lack of consideration of atmosphere conditions and source elevation in our model. Moreover, since the radiation pattern of the thunder source is unknown, the propagation path in the atmosphere may introduce the trade-

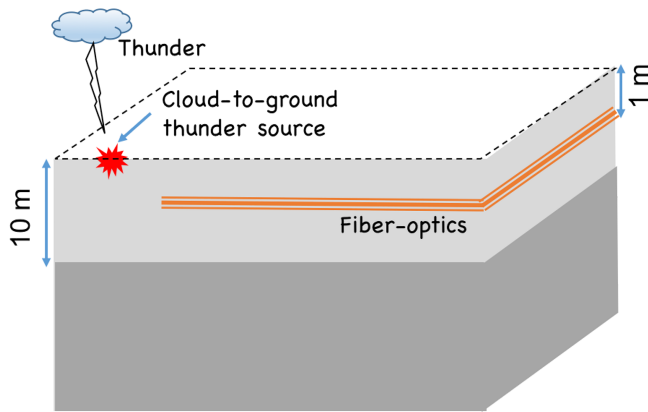


Figure 11. Layered model for synthesizing the thunder-induced signals recorded by the fiber.

off between the location and the original time in the LSLI, which could also contribute to the observed differences. Figure 10b zooms in on the locations of four events (e4, e5, e6, e7, and e9) closest to the DAS array. Except e6, the locations of other four are consistent with the lightning strike ones and their initial times (color in Figure 10b) are close.

4. Full Waveform Processing of DAS Data

We then demonstrate that the DAS full waveforms can be utilized to characterize the source. We take Events e6 and e7 as examples. First, we model full waveform DAS data by solving the SH (horizontally polarized shear wave) wave equation (Zhu & Harris, 2014). The two-layered model (see Figure 11) is used to generate shear wave (SH) wave propagation. The first layer thickness is 10 m with 420 m/s for e6 and 320 m/s for e7, while the second half space has velocities 510 and 400 m/s for e6 and e7, respectively. The 3-D model is discretized by $600 \times 600 \times 50$ with 5-m spacings in the x - y plane and 1-m spacing in depth. A free surface boundary condition is considered. The thunder event is modeled as a point pressure source excited on the ground. The source wavelet is the Ricker function with the dominate frequency 20 Hz. For multiple arrivals, we use a chain of delayed point sources of spherically expanding wave fronts as the thunder source suggested by a theoretical study (Few, 1969). The source location for e6 and e7 are estimated from the above location inversion.

The synthetic full waveform seismogram in Figure 12a shows a good agreement in kinematics and dynamics with the observed DAS data (Figure 12b). In particular, multiple arrivals of reverberated waves in the synthetic seismogram (normalized waveform) mimic Event e6 very well (arrows in Figure 12c) and significant reverberations are caused by a low seismic wave velocity in the first layer. The complicated waveforms across channels possibly due to the near-surface spatial heterogeneity are not well captured in synthetics.

The synthetic full waveform seismogram in Figure 12a shows a good agreement in kinematics and dynamics with the observed DAS data (Figure 12b). In particular, multiple arrivals of reverberated waves in the synthetic seismogram (normalized waveform) mimic Event e6 very well (arrows in Figure 12c) and significant reverberations are caused by a low seismic wave velocity in the first layer. The complicated waveforms across channels possibly due to the near-surface spatial heterogeneity are not well captured in synthetics.

Further, we use the hybrid multiplicative time-reversal imaging approach (Zhu et al., 2019) to characterize the thunder source. This method back propagates recorded data at an individual station or in a group of

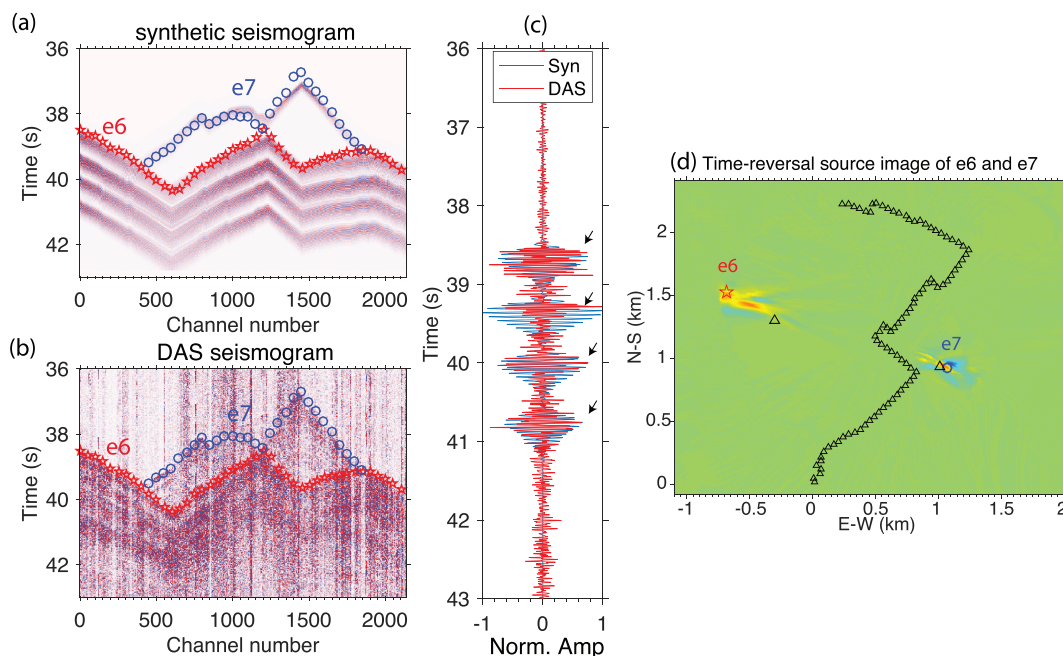


Figure 12. Full waveform processing of DAS array observations of Events e6 and e7. (a) Simulated full waveform. (b) DAS observed seismograms over all 2,137. The first arrival times of two events e6 (red stars) and e7 (blue circles) are overlaid on the seismograms. (c) Comparison of synthetic and DAS data trace (Channel 100). (d) The source image by time-reversal imaging of DAS observed seismograms in (b) where triangle symbols represent the possible events from NLDN.

stations at a predicted apparent velocity to focus all possible source locations on a prescribed spatiotemporal grid. Possible event locations in the grid are constructed by interfering back propagated wavefield. Zhu et al. (2019) showed that, in the same way, the multiplicative time-reversal imaging ensures better resolution than the time-reversal imaging method.

Due to the “zig-zag” shape of the DAS array, we split the DAS channels into three groups to separately back propagate the 1-s length windowed DAS seismograms (Channels 1 to 604, Channels 605 to 1226, and Channels 1441 to 2137). For each group, we compute the back propagated wavefield by solving the time-reversed acoustic wave equation. Then we multiply back propagated wavefields between three groups and stack in time to obtain the source image. The final imaged locations of two sources for Events e6 and e7 are shown in Figure 12d. The maximum amplitudes represent the possible locations that show consistency with the inverted location from the arrival time least squares inversion. The tails of the amplitude are likely caused by the waveform complexity with strong noise or scattering energy propagating in the near surface or the one-side array geometry.

5. Discussion and Conclusion

We have showed evidence of thunderstorm-induced seismic signals measured by a DAS array using a 4.2-km-long existing telecommunication fiber-optic cable. To our knowledge this is the first array of its kind deployed in a region, which regularly experiences thunder and lightning during storms. This report provides the first observations of thunder-induced ground motions at a DAS array of closely spaced sensors. The DAS array can record seismic waves caused by thunder sources with a good signal-to-noise ratio. Moreover, the higher fidelity DAS data can record the broadband thunder signals that peak from 20 to 130 Hz, which is consistent with previously published values by microphones, for example, 4 to 125 Hz (Holmes et al., 1971; Lacroix et al., 2018). While most of previous seismological studies focused on the infrasound bandwidth at frequencies lower than 20 Hz, the broadband nature of DAS data can be of great value for characterizing the audible thunder (higher than 20 Hz) that induce relatively small pressure variations from 0.2 to 2.4 Pa (Farges & Blanc, 2010) or even 40 Pa at several kilometers (Lacroix et al., 2018). In addition, the spatiotemporal variation of DAS data travel times allows us to compute the back azimuth and locations of thunder-seismic sources. The results indicate the path of the thunder-seismic sources as it moves from northwest to south to northeast.

In addition to evidence on thunder-induced seismic signals, we also observed the correlation between stacked DAS seismic energy and lightning current energy. This observation differs from previous thunderstorm observations using small array of microphones by Farges and Blanc (2010) and Lacroix et al. (2018) in which no correlation between acoustic energy and absolute value of lightning current in kiloamperes was found. They instead found a positive correlation with the charge moment change, which was considered to be more representative of the power of the full flash rather than the peak current which represents only the power inside the first microseconds of a return stroke. However, compared to limited distribution of microphones, total DAS seismic energy is calculated from stacking the strain rate DAS measurements across 4.2-km DAS arrays, which may be better suited to provide a high-fidelity record of the lightning stroke. This observed link may prove an opportunity to quantify the impact of thunderstorms on the ground using DAS fiber-optic arrays. Moreover, the dense DAS array with continuous records can constrain this energy transfer process between thunderstorm and ground motions in both temporal and spatial scales. This finding may open up the way of studying the coupling process between weather process and solid Earth.

An important advantage of high-dense DAS recordings is to enable data mining of full waveforms using exploration seismology processing techniques or machine learning (Martin et al., 2018). We demonstrated the full waveform modeling of DAS measurements and further used a state-of-art time-reversal migration to locate two sources. In addition, as qualitatively shown in Figure 4, the amplitude versus offset and spectrogram of Event e4 shows that waveforms are dispersive and attenuated around Channel 2000, which may indicate a more dispersive medium around the site Channel 2000. A pioneer study by Lin and Langston (2009b) used a seismometer-microphone recording of thunders to estimate substrate velocities and the average thickness and velocities of the near-surface layer. This could be particularly useful in the areas of less earthquake seismicity, for example, the eastern United States, where few local earthquakes are insufficient to constrain high-resolution images of the near surface and/or upper crust. DAS arrays can provide dense

recordings to detect thunder-induced Rayleigh wave sources and that dense array can provide advantages in verifying the source type (distinguishing from anthropogenic noise), imaging the source location, and estimating the Rayleigh wave velocity structure of the site. Looking forward, thunder-induced sources detected by widespread fiber networks could be an important seismic source for developing high resolution velocity models in the eastern United States. Our future work will investigate the use of DAS waveforms for characterization of thunder wave propagation and more detailed mapping of the near-surface velocity and attenuation structure for hazard analysis.

The results also suggest that DAS observations may be able to distinguish between cloud-to-ground and cloud-to-cloud lightning. The altitude of the cloud-to-cloud discharge could be from 5 to 10 km. A substantial part of the time of propagation is between the cloud and the ground at the speed of the sound. The estimated propagation velocity of e7 and e15 is close to the velocity of sound in comparison with the other 16 propagation velocities that are much faster. This result suggests that e7 and e15 may have been produced by cloud-to-cloud lightning, whereas the other strokes were produced by cloud-to-ground lightning. Additional observations would be needed to evaluate this hypothesis.

It is well known that urban areas can influence thunderstorms and their hazards (Niyogi et al., 2011; Reames & Stensrud, 2018). The DAS array may therefore be a useful data source for urban-scale thunder tracking, particularly because a DAS array can piggy-back on existing telecommunication fiber networks, making it much more cost-effective and practical in urban areas than installing new instrument arrays of other types.

Acknowledgments

We thank the Todd Myers and Ken Miller at Penn State University and Thomas Coleman from Silixa who help set up the fiber-optic DAS array at Penn State. We are indebted to Eileen Martin for her tremendous help on the project planning and tap tests and reviewing the manuscript. We also thank Vaisala for making the lightning strike data available to our research and Chuck Ammon and Ron Holle (Vaisala) for providing comments on an earlier version. This research was supported by Penn State Institute of Environment and Energy seed grant and Institute of Natural Gas Research. The DAS thunder waveform data are available via <https://sites.psu.edu/tzhu/foresee/> (at https://sites.psu.edu/tzhu/files/2019/11/PSUDAS.UTC_20190415_0330-45.rsrf.zip and https://sites.psu.edu/tzhu/files/2019/11/PSUDAS.UTC_20190415_0346-59.rsrf.zip). Broadband seismic waveform data for the PSRS station are retrieved from the IRIS Data Management Center (doi.org/10.7914/SN/PE).

References

- Ajo-Franklin, J. B., Dou, S., Lindsey, N. J., Monga, I., Tracy, C., Robertson, M., et al. (2019). Distributed acoustic sensing using dark fiber for near-surface characterization and broadband seismic event detection. *Scientific Reports*, 9(1), 1328. <https://doi.org/10.1038/s41598-018-36675-8>
- Assink, J. D., Evers, L. G., Holleman, I., & Paulssen, H. (2008). Characterization of infrasound from lightning. *Geophysical Research Letters*, 35, L15802. <https://doi.org/10.1029/2008GL034193>
- Daley, T. M., Freifeld, B. M., Ajo-Franklin, J. B., Dou, S., Pevzner, R., Shulakova, V., et al. (2013). Field testing of fiber-optic distributed acoustic sensing (DAS) for subsurface seismic monitoring. *The Leading Edge*, 32(6), 699–706. <https://doi.org/10.1190/tle32060699.1>
- Daley, T. M., Miller, D. E., Dodds, K., Cook, P., & Freifeld, B. M. (2016). Field testing of modular borehole monitoring with simultaneous distributed acoustic sensing and geophone vertical seismic profiles at Citronelle, Alabama. *Geophysical Prospecting*, 64(5), 1318–1334. <https://doi.org/10.1111/1365-2478.12324>
- Dou, S., Lindsey, N. J., Wagner, A. M., Daley, T. M., Freifeld, B., Robertson, M., et al. (2017). Distributed acoustic sensing for seismic monitoring of the near surface: A traffic-noise interferometry case study. *Scientific Reports*, 7(1), 11620. <https://doi.org/10.1038/s41598-017-119864>
- Ebeling, C. W., & Stein, S. A. (2011). Seismological identification and characterization of a large hurricane. *Bulletin of the Seismological Society of America*, 101(1), 399–403. <https://doi.org/10.1785/0120100175>
- Egorov, A., Correa, J., Bóna, A., Pevzner, R., Tertyshnikov, K., Glubokovskikh, S., et al. (2018). Elastic full-waveform inversion of vertical seismic profile data acquired with distributed acoustic sensors. *Geophysics*, 83(3), R273–R281. <https://doi.org/10.1190/geo2017-0718.1>
- Farges, T., & Blanc, E. (2010). Characteristics of infrasound from lightning and sprites near thunderstorm areas. *Journal of Geophysical Research*, 115, A00E31. <https://doi.org/10.1029/2009JA014700>
- Few, A. A. (1969). Power spectrum of thunder. *Journal of Geophysical Research*, 74(28), 6926–6934. <https://doi.org/10.1029/jc074i028p06926>
- Few, A. A. (1970). Lightning channel reconstruction from thunder measurements. *Journal of Geophysical Research*, 75(36), 7517–7523. <https://doi.org/10.1029/JC075i036p07517>
- Gerstoft, P., Fehler, M. C., & Sabra, K. G. (2006). When Katrina hit California. *Geophysical Research Letters*, 33, L17308. <https://doi.org/10.1029/2006GL027270>
- Gualtieri, L., Camargo, S. J., Pascale, S., Pons, F. M., & Ekström, G. (2018). The persistent signature of tropical cyclones in ambient seismic noise. *Earth and Planetary Science Letters*, 484, 287–294. <https://doi.org/10.1016/j.epsl.2017.12.026>
- Holmes, C. R., Brook, M., Krehbiel, P., & McCrory, R. (1971). On the power spectrum and mechanism of thunder. *Journal of Geophysical Research*, 76, 2106–2115. <https://doi.org/10.1029/JC076i009p02106>
- Jousset, P., Reinsch, T., Ryberg, T., Blanck, H., Clarke, A., Aghayev, R., et al. (2018). Dynamic strain determination using fibre-optic cables allows imaging of seismological and structural features. *Nature Communications*, 9(1), 2509. <https://doi.org/10.1038/s41467-018-04860-y>
- Kappus, M. E., & Vernon, F. L. (1991). Acoustic signature of thunder from seismic records. *Journal of Geophysical Research-Atmospheres*, 96, 10,989–11,006. <https://doi.org/10.1029/91jd00789>
- Lacroix, A., Farges, T., Marchiano, R., & Coulouvrat, F. (2018). Acoustical measurement of natural lightning flashes: Reconstructions and statistical analysis of energy spectra. *Journal of Geophysical Research. Atmospheres*, 123, 12,040–12,065. <https://doi.org/10.1029/2018JD028814>
- Lin, T.-L., & Langston, C. A. (2007). Infrasound from thunder: A natural seismic source. *Geophysical Research Letters*, 34, L14304. <https://doi.org/10.1029/2007GL030404>
- Lin, T.-L., & Langston, C. A. (2009a). Ground motions induced by thunder: 1. Observations. *Journal of Geophysical Research*, 114, B04303. <https://doi.org/10.1029/2008JB005769>
- Lin, T.-L., & Langston, C. A. (2009b). Thunder-induced ground motions: 2. Site characterization. *Journal of Geophysical Research*, 114, B04304. <https://doi.org/10.1029/2008JB005770>

- Lindsey, N. J., Martin, E. R., Dreger, D. S., Barry, F., Stephen, C., James, S. R., et al. (2017). Fiber-optic network observations of earthquake wavefields. *Geophysical Research Letters*, 44, 11,792–11,799. <https://doi.org/10.1002/2017GL075722>
- Martin, E. R., Huot, F., Ma, Y., Cieplicki, R., Cole, S., Karrenbach, M., & Biondi, B. L. (2018). A seismic shift in scalable acquisition demands new processing: Fiber-optic seismic signal retrieval in urban areas with unsupervised learning for coherent noise removal. *IEEE Signal Processing Magazine*, 35(2), 31–40. <https://doi.org/10.1109/MSP.2017.2783381>
- Martin, E. R., Lindsey, N. J., Ajo-Franklin, J. B., & Biondi, B. L. (2019). Introduction to interferometry of fiber optic strain measurements, *EarthArXiv*. <https://doi.org/10.31223/osf.io/s2tjd>
- Mateeva, A., Lopez, J., Potters, H., Mestayer, J., Cox, B., Kiyashchenko, D., et al. (2014). Distributed acoustic sensing for reservoir monitoring with vertical seismic profiling. *Geophysical Prospecting*, 62, 679–692. <https://doi.org/10.1111/1365-2478.12116>
- Menke, W. (2012). *Geophysical data analysis: Discrete inverse theory*. Amsterdam: Elsevier/Academic Press.
- Murphy, M. (2018). Locating lightning. *Physics Today*, 71(3), 32. <https://doi.org/10.1063/PT.3.3869>
- Nag, A., Murphy, M. J., Schulz, W., & Cummins, K. L. (2015). Lightning locating systems: Insights on characteristics and validation techniques. *Earth and Space Science*, 2. <https://doi.org/10.1002/2014EA000051>
- Niyogi, D., Pyle, P., Lei, M., Arya, S. P., Kishtawal, C. M., Shepherd, M., et al. (2011). Urban modification of thunderstorms: An observational storm climatology and model case study for the Indianapolis urban region. *Journal of Applied Meteorology and Climatology*, 50, 1129–1144. <https://doi.org/10.1175/2010JAMC1836.1>
- Reames, L. J., & Stensrud, D. J. (2018). Influence of a Great Plains urban environment on a simulated supercell. *Monthly Weather Review*, 146, 1437–1462. <https://doi.org/10.1175/MWR-D-17-0284.1>
- Retailleau, L., & Gualtieri, L. (2019). Toward high-resolution period-dependent seismic monitoring of tropical cyclones. *Geophysical Research Letters*, 46. <https://doi.org/10.1029/2018GL080785>
- Spikes, K. T., Tisato, N., Thomas, E. H., & Holt, J. W. (2019). Comparison of geophone and surface-deployed distributed acoustic sensing seismic data. *Geophysics*, 84(2), A25–A29. <https://doi.org/10.1190/geo2018-0528.1>
- Tanimoto, T., & Lamontagne, A. (2014). Temporal and spatial evolution of an on-land hurricane observed by seismic data. *Geophysical Research Letters*, 41(21), 7532–7538. <https://doi.org/10.1002/2014gl061934>
- Wang, H. F., Zeng, X., Miller, D. E., Fratta, D., Feigl, K. L., Thurber, C. H., & Mellors, R. J. (2018). Ground motion response to an ML 4.3 earthquake using co-located distributed acoustic sensing and seismometer arrays. *Geophysical Journal International*, 213(3), 2020–2036. <https://doi.org/10.1093/gji/ggy102>
- Yu, C., Zhan, Z., Lindsey, N. J., Ajo-Franklin, J. B., & Robertson, M. (2019). The potential of DAS in teleseismic studies: Insights from the Goldstone experiment. *Geophysical Research Letters*, 46, 1320–1328. <https://doi.org/10.1029/2018GL081195>
- Zeng, X., Lancelle, C., Thurber, C., Fratta, D., Wang, H., Lord, N., et al. (2017). Properties of noise cross-correlation functions obtained from a distributed acoustic sensing array at Garner Valley, California. *Bulletin of the Seismological Society of America*, 107(2), 603–610. <https://doi.org/10.1785/0120160168>
- Zhang, J., Gerstoft, P., & Bromirski, P. D. (2010). Pelagic and coastal sources of P-wave microseisms: generation under tropical cyclones. *Geophysical Research Letters*, 37(15). <https://doi.org/10.1029/2010GL044288>
- Zhu, T., & Harris, J. M. (2014). Modeling acoustic wave propagation in heterogeneous attenuating media using decoupled fractional Laplacians. *Geophysics*, 79(3), T105–T116. <https://doi.org/10.1190/geo2013-0245.1>
- Zhu, T., Sun, J., Gei, D., Carcione, J. M., Cance, P., & Huang, C. (2019). Hybrid multiplicative time-reversal imaging reveals the evolution of microseismic events: Theory and field data tests. *Geophysics*, 84(3), KS71–KS83. <https://doi.org/10.1190/geo2018-0662.1>